Absorption and luminescence studies of free-standing porous silicon films

Y. H. Xie, M. S. Hybertsen, and William L. Wilson
AT&T Bell Laboratories, Murray Hill, New Jersey 07974

S. A. Ipri
Department of Material Science, University of Illinois, Urbana, Illinois 61801

G. E. Carver
AT&T Bell Laboratories, Engineering Research Center, Princeton, New Jersey 08540

W. L. Brown, E. Dons, B. E. Weir, A. R. Kortan, G. P. Watson, and A. J. Liddle
AT&T Bell Laboratories, Murray Hill, New Jersey 07974
(Received 27 October 1993)

The result of a combined study of the absorption and photoluminescence (PL) from high-optical-quality free-standing porous Si films is presented. These films, which have a scattering loss less than 10%, allow unambiguous, detailed study of the system's absorption edge and, in addition enable us to correlate the absorption and emission behavior on the same sample. H-ion scattering and H forward recoil data are used to accurately determine the bulk equivalent thickness to allow extraction of the absorption coefficient. X-ray diffraction, in conjunction with transmission electron microscopy, are utilized to measure the lattice constant and to confirm the crystalline nature of the structure. The combined photoluminescence and absorption studies are used to examine the relative energy shift of the luminescence peak with respect to that of the absorption edge. It is shown that the absorption begins coincident in energy with the photoluminescence peak, rising smoothly over a range of 1–2 eV. More importantly, the absorption is very weak in the region of the PL in comparison to a direct-gap semiconductor, indicative of the intrinsically weak oscillator strength. An effective-mass-based model for an ensemble of Si nanocrystallites is compared to the experimental results. Phonon-assisted transitions dominate the optical processes. The results support the picture that the absorption derives primarily from the interior states of nanocrystalline Si particles of characteristic dimension below 100 Å. The dynamics of the photoluminescence are reexamined and found to be consistent either with recombination between interior electron and hole states, of the Si nanocrystallites, or involving shallow trap states.

I. INTRODUCTION

The observation of visible luminescence with a few percent quantum efficiency at room temperature from porous Si (PS) (Ref. 1) prompted renewed hope for the possible development of Si-based light-emitted devices. The question of whether the material offers realistic potential for such an electronically injected emission device, however, cannot be answered without a thorough understanding of the band structure and the luminescence mechanism of this material. Of the several luminescence schemes that have been proposed to date, the quantum confined Si-nanocluster model appears to be the most consistent based on two sets of experiments that effectively rule out siloxene hypothesis.[2,3] Experiments showing signatures of Si phonons have provided evidence that the luminescence involves regions of nanocrystalline Si.[4,5] In addition, recent photoluminescence (PL) with characteristics similar to those of porous Si have been observed from artificially synthesized Si nanoclusters.[6,7]

Despite these experimental results, controversies still exist. Models of luminescence from hydride Si (Ref. 8) and from an amorphous phase Si (Ref. 9) that are backed by self-consistent experimental evidence have been proposed. Questions naturally arise from such controversies as to whether there is more than one luminescence mechanism, or if some of the experimental results are subject to alternative interpretations. The fact that the luminescence process probes mainly relaxed energy states and is subject to strong influence from nonradiative recombination paths is one of the major reasons for the confusion. It has become more apparent that in order to obtain a clear understanding of the band structure of porous Si, absorption properties that relate directly to the oscillator strength will have to be studied in conjunction with luminescence. Understanding this correlation is also quite important for evaluating recent proposals for the role of trap states in the luminescence process.[10]

Here we report the results of combined direct absorption and luminescence studies in an effort to probe the energy band structure as well as the luminescence mechanism. The present samples are free-standing PS films with the good optical quality (scattering loss less than 10%) which exhibit visible photoluminescence upon UV excitation. The bulk equivalent thickness and the density of the films are determined by the combination of H-ion scattering, H forward recoil, and cross-sectional scanning electron microscopy (XSEM). X-ray diffraction is used in conjunction with transmission electron microscopy to measure the lattice constant and to determine if the

structures are crystalline. Combined photoluminescence and absorption measurements are used to examine the relative energy shift of the luminescence peak with respect to that of the absorption edge.

Direct absorption experiments on PS have been reported in the literature.[10–13] However, the combination of absorption and photoluminescence measurements here allow examination of the correlation between the two on samples of high optical uniformity. This increases the probability that the observed absorption and luminescence are indeed from the same microstructures. We discuss the degree to which the nanocrystallite model can coherently explain the available data and explore the ramifications of this picture. Despite the complexity of the luminescence dynamics, which may well be due to the role of shallow traps,[10] this model is a consistent framework to describe the optical properties of porous Si. On this basis, we can foresee potential, fundamental limitations on the application of porous Si for optoelectronic applications.

II. EXPERIMENTS

The PS samples were prepared from Si(100) wafers with p-type doping of 0.08–0.1 Ω cm resistivity. The wafer is placed in an electrochemical cell with a portion of the polished surface exposed to the electrolyte of 20 wt.% HF (mixture of three portions of methyl alcohol with two portions of concentrated, 50 wt.%, HF). The Si wafer was biased as the anode and a Pt electrode was used as the cathode. At the end of the porous film formation, the anodization current density was quickly increased to 300 mA/cm^2 and the reaction turned into electrochemical polishing which separated the PS film from the substrate. All the samples were fabricated in the dark. We are only able to find a fairly narrow parameter window for the fabrication. Outside this window, the films either break up into thin shreds upon drying, or have extremely low luminescence yield. This is the main reason why we could not get transparent films with higher quantum efficiency (as will be seen later). Details of the preparation and physical properties of the films are given in Table I. The films show an amber color as prepared, and are very transparent to the eye. The films do break up upon separation from the substrate, and the typical sizes are on the order of 1 cm^2.

The absorption measurements were performed on a HP8452A diode array spectrophotometer. In order to deduce the physically meaningful absorption coefficient α from the absorption data, the bulk equivalent thickness of the PS film needs to be determined accurately. The combination of H-ion scattering and H forward recoil were used to measure the sheet density of Si in the PS samples and, hence, yield the fraction f of the sample occupied by Si. The reason that a H forward recoil experiment is needed is that as-fabricated samples contain up to 30% H which, if not included, can cause a significant misinterpretation of the Si sheet density. The H-ion scattering experiment was done using 1.4 MeV H ions in place of He ions in an otherwise conventional Rutherford backscattering setup. The increased penetration depth of H ions over that of He ions enables measurements at these large sample thicknesses.

TABLE I. Parameters characterizing the two samples discussed in this paper: anodization current density J; anodization time t; film thickness d; effective film thickness d_{eff}; and fraction of Si in film f.

Sample	J mA/cm^2	t min	d μm	d_{eff} μm	f
1	10	30	18.3	5.5	0.30
2	20	7	7.9	2.1	0.27

The luminescence properties of these PS films were studied using both steady-state as well as temporally and spatially resolved emission techniques. The steady-state PL measurements at 300 K were performed on a SPEX Flourolog spectrometer with a Hg arc lamp as the excitation source and a photon-counting photomultiplier tube as the detector. Both the excitation and the emission spectrometers in this instrument are 0.5 m with 1200 line/mm gratings. All data were corrected to compensate for the spectrometer response. The excitation wavelength was 350 nm for the steady-state PL studies. For temperature-dependent data, the films were mounted between single-crystal sapphire flats in an Air Products continuous-flow liquid-helium cryostat that was equipped with variable temperature electronics. The time-resolved emission data were taken using a Continuum model RGA500 Nd YAG regenerative amplifier as an excitation source. The laser's output pulses were 60 ps in duration at 1064 nm. The amplifier output was frequency tripled using a β barium borate crystal, attenuated and focused to a 1 mm spot on the film. The broad emission was collected and imaged through a 0.25-m monochrometer onto a fast photomultiplier tube. The system time resolution was 10 ns with a 6-nm spectral bandpass. The transients were averaged on a LeCroy 7200, 500 MHz, precision digital oscilloscope. The spatially resolved PL (SRPL) (Ref. 14) scans were taken by pumping the sample with a 514-nm argon laser beam focused to a 1-μm spot. The spot is raster scanned over a 250×200 μm^2 field. Broadband luminescence is collected at wavelengths longer than 700 nm, and detected by a Ge photodiode. Signals are then digitized and displayed on a video monitor. Scans were taken in both plan and edge views.

X-ray diffraction was utilized to determine whether the PS samples are crystalline. The x-ray analysis was done on a 12 kW rotating anode generator equipped with a triple-axis goniometer monochromator in single-crystal geometry with a resolution of 10^{-3} Å^{-1}. Transmission electron microscopy (TEM) was used in conjunction with the x-ray diffraction to examine the microstructure of the PS samples. The TEM analysis was carried out using the free-standing films without further sample preparation. Both the phase-contrast image and the diffraction pattern were taken with the electron beam penetrating the thin portion at the edges of a tilted PS film.

A majority of the analyses were performed within hours of the sample preparation to minimize oxidation. One noticeable exception was the TEM analysis, which was done after the sample was exposed to air for about a month. This point should be kept in mind when inter-

preting the TEM result, in which an oxide layer appeared to exist, especially in the discussion section.

III. THEORETICAL MODEL

We consider the predictions of the nanocrystallite model for porous Si which is modeled by an ensemble of nanocrystallites or quantum dots. In general terms, absorption and emission will take place both through pseudodirect terms, allowed because the finite size of the crystallites breaks the bulk-crystal momentum selection rule, and also through the usual phonon-assisted processes. A unified model including both contributions in an effective-mass approach has been given.[15]

The imaginary part of the dielectric function, which describes the light-induced electronic transitions in a homogeneous array of crystallites has several terms:

$$\varepsilon''(\omega)=\frac{8\pi^2e^2}{m_e^2\omega^2}N_c\sum_{e,h}\left\{|p_{eh}^{(1)}|^2\delta(E_e+E_h+E_g-\hbar\omega)+\sum_{\lambda\mathbf{q}}|p_{eh,\lambda\mathbf{q}}^{(2)}|^2\right.$$
$$\times[1+n_{\lambda\mathbf{q}})\delta(E_e+E_h+E_g+\hbar\omega_{\lambda q}-\hbar\omega)$$
$$\left.+n_{\lambda q}\delta(E_e+E_h+E_g-\hbar\omega_{\lambda\mathbf{q}}-\hbar\omega)]\right\}, \quad (1)$$

where N_c is the density of crystallites in the sample. The labels e,h index the low-lying empty and occupied states of the crystallite, which have energies $E_{e,h}$ relative to the respective bulk band edges. The bulk band gap is E_g. The zero-phonon or pseudodirect transitions are described by the matrix element $p_{eh}^{(1)}$ which includes the selection rules. The phonon degrees of freedom are indexed by $\lambda\mathbf{q}$ and the second-order matrix element $p_{eh,\lambda\mathbf{q}}^{(2)}$ must include the relevant electron-phonon coupling. At finite temperature, there is both a phonon emission and a phonon absorption term, governed by the phonon occupancy $n_{\lambda\mathbf{q}}$.

To analyze the absorption and emission, we adopt an effective-mass model to represent the electron valleys in Si, located along the x, y, and z orientations in momentum space, near the zone edges, as well as the hole states near the zone center. The crystallites are modeled by near-cubic quantum boxes with faces of (001) symmetry. This assumed shape should not alter our general conclusions, but does simplify the analysis. The quantum boxes are generally terminated by hydride or oxide which we model by a finite barrier for electrons or holes. Details of the model and calculations are given in the Appendix. It is difficult to quantify the limitations, but one in general expects that such an effective-mass model will lose accuracy as the length scale becomes as small as 15–20 Å. The model does provide a reliable, semiquantitative guide.

The ensemble of crystallites is described by a size distribution

$$P(L)\propto L^2e^{-(L-L_0)^2/\delta L^2}. \quad (2)$$

The expected size distribution is often analyzed on the basis of the photoluminescence spectrum. However, given the rather low efficiencies observed in the luminescence, this could be misleading. The goal is to compare the luminescence and absorption for the same distribution. Usually, the efficiency is given by the ratio $W_{\rm rad}/(W_{\rm rad}+W_{\rm nr})$. Given uncertainties about the mechanism for the time domain decay of the luminescence, we adopt a simpler model to get the radiative fraction. If there is, on average, one fast trap per unit volume L_c^3, then the probability that a given crystallite of volume L^3 will have no traps, and hence radiate, is simply given by Poisson statistics

$$P_{\rm rad}(L)=e^{-L^3/L_c^3}. \quad (3)$$

From this model, the optical properties of the ensemble can be calculated as an average and the luminescence spectrum as a function of energy can be obtained. Since we consider $T=300$ K, subtleties associated with the low-energy exciton manifold are not important, and the details, which can lead to the very slow luminescence at low temperature,[4] can be ignored. The phonon-assisted transitions dominate in the energy range of the red emission seen in the present samples, as discussed in detail elsewhere.[15]

In order to compare with the data, the dielectric-function characteristic of the crystallites must be related to a macroscopic dielectric function ε_m. This depends on the porosity, or relative fraction f of the sample occupied by crystallites. We use the effective medium theory described by Bottcher and Bordewijk,[16] assuming that the balance of the sample is vacuum. Then the relationship used is just

$$\frac{\varepsilon_m-1}{3\varepsilon_m}=f\frac{\varepsilon-1}{2\varepsilon_m+\varepsilon}. \quad (4)$$

The local field inside a crystallite differs substantially from the average, macroscopic field. Near the threshold $\varepsilon''\ll\varepsilon'$, so it is straightforward to correct the absorption and emission. This introduces a local-field correction factor for both the calculated absorption, and the spontaneous emission rate:

$$\alpha_m(\omega)=\frac{\omega}{n_mc}F(\varepsilon,\varepsilon_m)f\varepsilon''(\omega), \quad (5a)$$

$$W_{sp}(\omega)=n_mF(\varepsilon,\varepsilon_m)\frac{2}{3}\omega\frac{e^2}{\hbar c}\frac{|p_{eh}^{(j)}|^2}{m_0^2c^2}. \quad (5b)$$

Here, the spontaneous emission rate is indicated for a particular recombination channel, which may or may not involve phonons. Expressions for the matrix element,

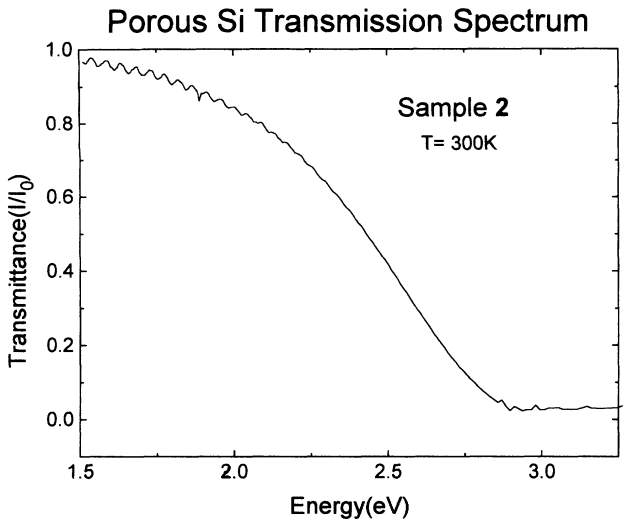

FIG. 1. Transmittance versus photon energy for sample 2 at 300 K.

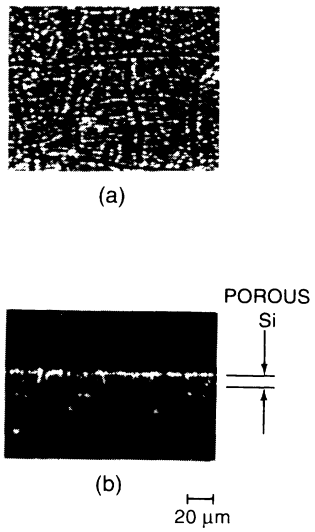

FIG. 3. Spatially resolved photoluminescence (SRPL) scans of a typical porous Si sample which is to lifted off from the substrate; (a) surface scan and (b) edge scan.

$p_{eh}^{(j)}$, in different cases appear in the Appendix. The calculated absorption coefficients and radiative recombination times presented here include the local field factor based on $\varepsilon'(\omega)$ for bulk Si and the measured fraction f. The factor F takes values in the range 0.2–0.3 for $f=0.25$–0.30 appropriate to many porous Si samples. Note that the effective absorption presented experimentally corresponds to dividing out f in Eq. (5a), which is also done for the calculated absorption.

IV. RESULTS

Figure 1 illustrates the high optical quality of the films studied. There is very low optical loss due to minimal scattering in the film. Aside from the fact that the absorption edge is noticeably blueshifted from that of bulk Si, the important feature to notice in Fig. 1 is that the transmittance is over 90% at the long-wavelength end of the spectrum which puts the upper limit on the combined scattering and reflection loss at less than 10%.

In addition to the low scattering loss, the films are very uniform to the eye when viewed in transmission. Since uniformity is such an important issue when interpreting the result of a combined study using various experimental techniques, we utilize SRPL to examine the uniformity of the luminescence relative to the transmission measurements. The SRPL results of sample 1 are presented in Fig. 2 with the surface and edge scans shown in Figs. 2(a) and 2(b), respectively. Aside from some debris, both scans show that the luminescence is very uniform throughout the volume of the porous Si film. In comparison, the same surface and edge scans of a more typical porous Si film (not lifted off from the substrate in this

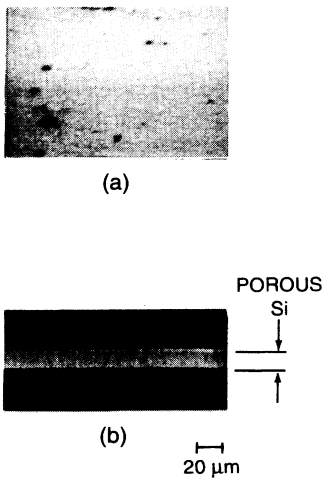

FIG. 2. Spatially resolved photoluminescence (SRPL) scans of sample 1, (a) surface scan, and (b) edge scan.

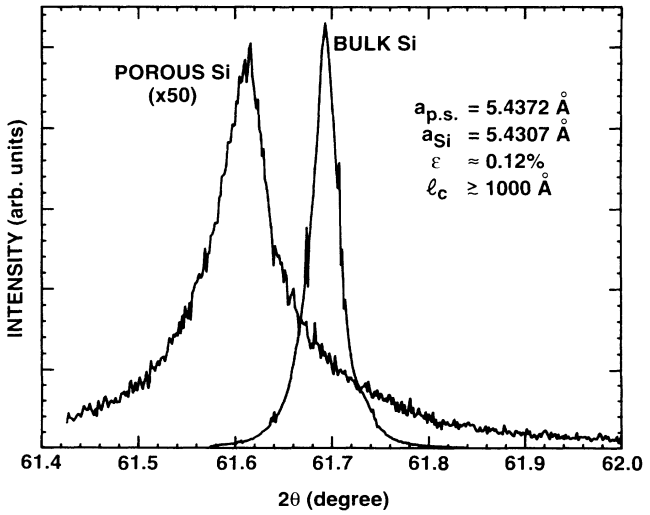

FIG. 4. X-ray θ–2θ scan of sample 1. A scan of the Si substrate from which sample 1 is prepared is also shown for reference.

case) are shown in Figs. 3(a) and 3(b). Figure 3(a) shows an extremely nonuniform luminescence under the surface scan. For the edge scan, Fig. 3(b) shows that most of the emission originates within the top 3–5 μm of the PS layer. SRPL images similar to those in Fig. 3 are quite typical among PS samples prepared with various recipes.[17] It is clear that a combined study of a nonuniform sample with a variety of experimental techniques could lead to erroneous conclusions if the nonuniformity is not taken into consideration. By the same token, the observed uniformity in the present samples gives confidence that the various techniques we use to examine the PS films are most likely to be probing the same microscopic mechanism that is related to the light emission.

With the above points in mind, we examined the crystallinity of the films. Figure 4 shows the x-ray θ–2θ scans of sample 1. There are two important features to notice: the position and the full width at half maximum (FWHM) of the sample 1 peak relative to that of the bulk Si crystal. From the peak position shift, a lattice dilation of $\approx 0.12\%$ in the direction perpendicular to the sample surface is obtained. The 0.12% strain, however, is too small to make any significant contribution to the position of the energy levels. From the FWHM of the porous Si peak, we obtain a correlation length of ≈ 1000 Å, a number that is too large to account for the blueshift of the absorption edge of the films. This discrepancy is resolved using TEM as shown below.

Figure 5 is the phase-contrast TEM micrograph of sample 1 with the inset showing the restricted beam diffraction. No clusters with size larger than 100 Å are observed. The average size is around 60 Å. The diffraction pattern shows that these nanoclusters are Si crystallites with long-range coherency (single crystal versus polycrystal diffraction patterns). The coherency range is given by the sampling volume of the electron beam which is composed of an area of $\approx 400 \times 400$ Å in cross section, and a sample thickness of ≈ 600 Å. This result agrees qualitatively with the 1000-Å x-ray correlation length.

The bulk equivalent thicknesses and the densities of the films are measured with a combination of H forward recoil, H-ion scattering, and XSEM. The result shows that sample 1 has a bulk equivalent thickness of 5.5 μm and a density of 30% of bulk Si; the corresponding values for sample 2 are 2.1 μm and 27%.

The measured density is closely related to the dielectric properties of the porous Si film. The Fabry-Perot oscillations in the spectrum shown in Fig. 1 can be used to deduce the effective index of refraction of the film. For sample 2, for example, the physical thickness of the film is 7.9 μm, and we obtain $n = 1.6 \pm 0.2$ for λ in the range ≈ 7200 Å to $\lambda \approx 8000$ Å. This can be compared to the macroscopic refractive index calculated from the effective medium theory, Eq. (4). For $\lambda \approx 800$ nm, $\varepsilon' = 13.5$ for bulk Si.[18] Using $f = 0.27$ for sample 2, this implies $n_m = 1.51$, in very good agreement with the value inferred from the interference oscillations.

The PL spectra for our samples (Fig. 6) are very similar in shape to those found in the literature. The peaks are somewhat to the red of those frequently reported. We have also measured the quantum efficiency of sample 1. The result is $\approx 0.13\%$, about one order of magnitude lower than the commonly quoted value of a few percent.

The quantitative measurement of the bulk equivalent thickness enables us to deduce the bulk equivalent absorption coefficient. The bulk equivalent absorption coefficient relates closely to the absorption mechanism and is a better measurement of the oscillator strength than the apparent absorption coefficient. The cluster-size distribution would have to be known before a cluster-size-dependent absorption coefficient could be deduced.

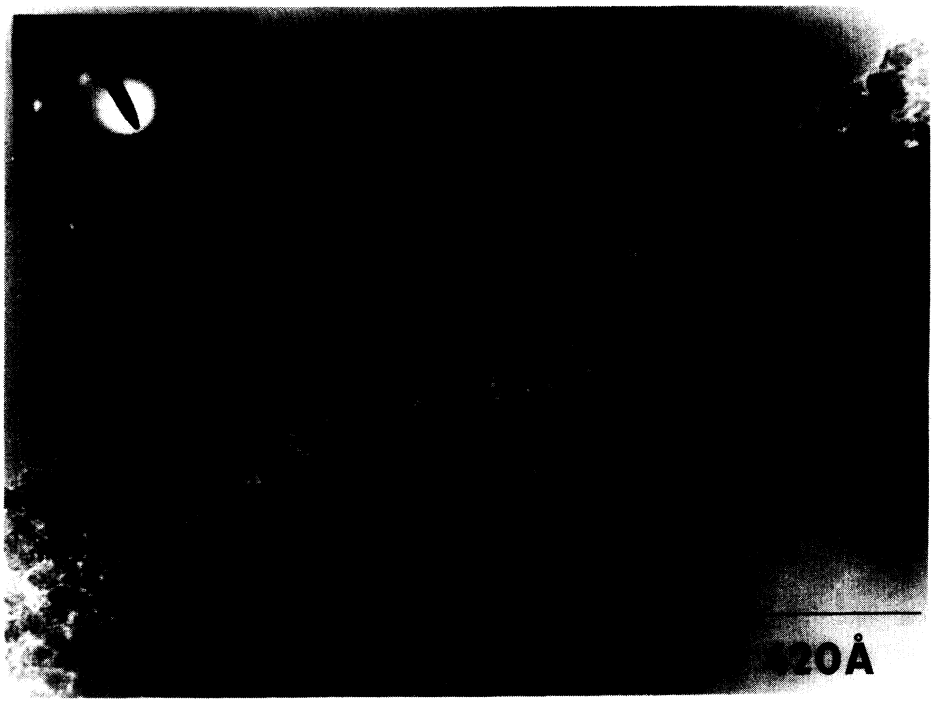

FIG. 5. Phase-contrast transmission electron micrograph of sample 1. The inset shows the diffraction pattern obtained when the beam is restricted to the thin portion of the sample, and its axis is rotated with respect to the micrograph as the result of the electron microscope "lens twist."

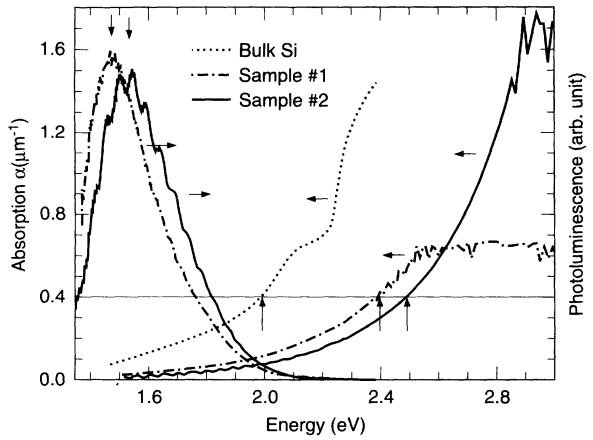

FIG. 6. Photoluminescence and absorption coefficient for samples 1 and 2 measured at 300 K. The excitation wavelength for the photoluminescence is 350 nm.

Figure 6 shows the bulk equivalent absorption data (Fig. 1 replotted on energy axis) for samples 1 and 2. Also plotted is the absorption coefficient for bulk Si.[18] The high-energy plateau in the absorption curves is unphysical, representing the region where the transmitted light intensity fell below the detector limit of the diode array spectrometer. To facilitate the quantitative discussion of the energy shift in absorption, we arbitrarily draw a horizontal line at $\alpha=0.4\ \mu m^{-1}$ and the intersections of this line with the absorption curves (as marked by the arrows) are used to measure the energy shift. Both the PL peak position and the absorption edge are blueshifted by ≈ 400 meV from that of bulk Si. This result qualitatively agrees with the quantum-confined Si cluster model in which luminescence is band to band or through localized states close to band edges. The fact that both the PL peak position and the absorption edge of sample 2 (higher porosity) are further blueshifted from that of sample 1 lends added support to this model, and agrees with the observation by Kanemitsu, Uto, and Masumoto.[13] In addition to the blueshift of both the PL and the absorption edge, it is important to notice that the absorption coefficient at the PL peak position is small but nonzero. The absorption rises smoothly and there is no absorption threshold at energies above the PL peak position. The shape of the absorption curves fits well to an exponential, being quite close to a straight line on a semilogarithmic plot. This is similar to the results from photothermal displacement spectroscopy, consistent with band-tail-type absorption.[10] The characteristic energy scale depends on the sample and the degree of blueshift, but is generally around 0.3 eV.

The calculated crystallite size dependence of the optical response is illustrated in Fig. 7. The imaginary part of the dielectric function is shown for essentially a single size of crystallite in each case. The calculation is done for a dense set of crystallites, e.g., $N_c=1/\Omega$ in Eq. (1) where Ω is the crystallite volume. The crystallites are cubic with a Gaussian distribution of size L which allows only for ± 1-Å variations. For the smallest size 30 Å, there is clear evidence for some of the discrete transitions expected from the confinement. As the size is increased, the curves systematically redshift, and become smoother. The large size limit reproduces the bulk response (Appendix). The signatures of the quantization due to finite size are the shift in threshold and the smaller overall magnitude as compared to the bulk limit. This also comes about from the discrete energy levels caused by confinement. The joint density of states in the low-energy range is reduced, or more correctly, has been shifted to higher energy.

We do not get an explicit size distribution from the experimental data. However, it is very interesting to see the predictions of a simple, plausible distribution. Using the model described by Eqs. (2) and (3) in Sec. III, the absorption and PL have been calculated for two different distributions designed to roughly reproduce the experimental situation for the two samples. The results are

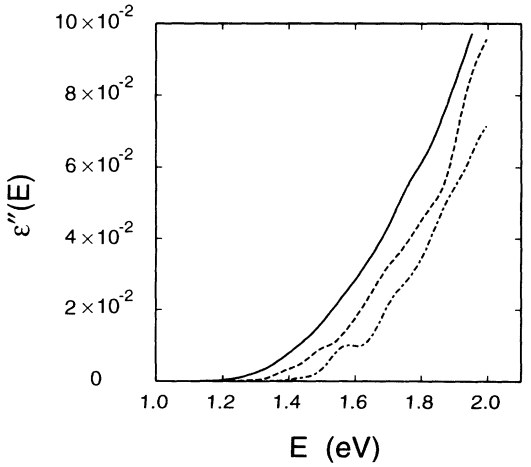

FIG. 7. Calculated imaginary part of the dielectric function as a function of energy for Si nanocrystallite of dimension 30 Å (dash-dotted line), 40 Å (dashed line) and 60 Å (solid line). The curves include a broadening with a 0.08-eV Gaussian, full width at half maximum.

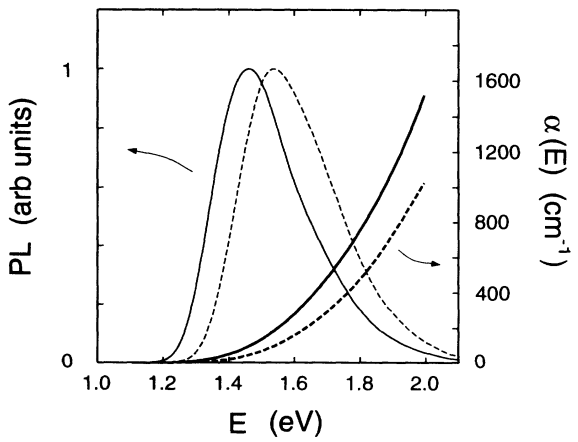

FIG. 8. Calculated effective absorption and luminescence as a function of energy for 2 Gaussian ensembles of Si nanocrystallite described in the text: average size of 34 Å (solid lines) and 41 Å (dashed lines).

shown in Fig. 8. The solid line is for the case $L_0=41$ Å, $\delta L=11$ Å, and $L_c=20$ Å with $f=0.30$. This yields a peak in the luminescence near 1.45 eV and an efficiency of about 0.5%. The calculated absorption near 2 eV is approximately 1600 cm^{-1}. The dashed line corresponds to $L_0=34$ Å, $\delta L=8$ Å, and $L_c=18$ Å with $f=0.25$. The calculated absorption near 2 eV is reduced to about 1000 cm^{-1}. The peak in the luminescence shifts upward by about 0.1 eV and the absorption curve also shifts to the blue. About half of the apparent blueshift of the absorption curve traces to the change in the local field factor F in Eq. (5a) according to the reduced density of crystallites, f. In both cases, the absorption smoothly rises from the region of the luminescence, with no significant features in the spectrum, and is close to the magnitude observed in Fig. 6 for $E=2$ eV. The present choice of a Gaussian size distribution does not reproduce the observed exponential shape of the absorption. The calculated absorption is too small by about a factor of 2 at $E=1.5$ eV. A different distribution, e.g., a simple exponential, which includes a tail with more larger scale crystallites can give more absorption at lower energy.

In the present model, the small luminescence efficiency implies that only a small fraction of the distribution can emit, according to Eq. (3). This is illustrated in Fig. 9 where it is seen that the emitting particles are only those in the extreme small size tail of the distribution. Thus, in this model, the luminescence lineshape on the blue side is related to the size distribution, and the luminescence lineshape on the red side is determined by the assumptions concerning the radiative fraction of the Si nanoclusters.

The temperature dependence of the PL of sample 1 is shown in Fig. 10. Figure 10(a) shows the PL spectra at 10 and 295 K, and Fig. 10(b) shows the detailed temperature dependence of the intensity at four wavelength windows on the PL spectrum. The temperature change causes the intensity, but not the spectral shape, to vary. The intensity increases with decreasing temperature, and

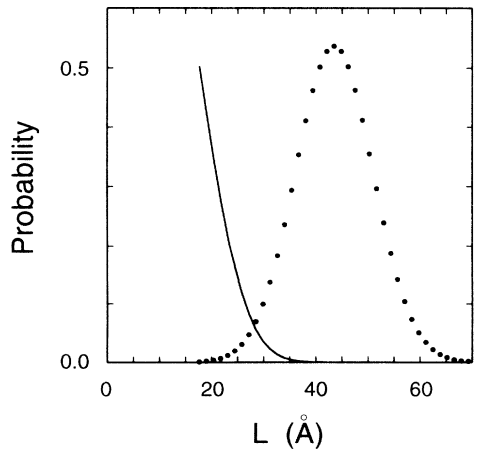

FIG. 9. The size distribution for an ensemble of crystallites of average size 41 Å following Eq. (2), normalized to number per 10 Å (solid circles) and the probability of radiating for $L_c=20$ Å, following Eq. (3) (line).

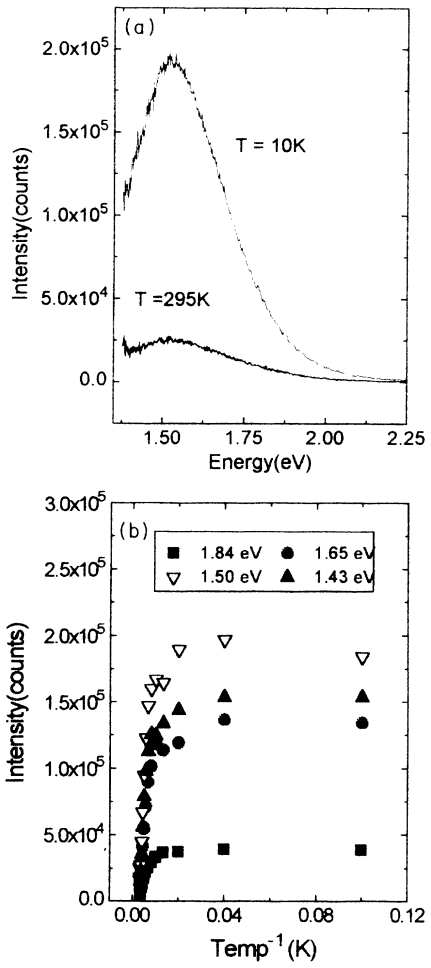

FIG. 10. (a) Photoluminescence spectra of sample 1 at 295 and 10 K. (b) The temperature dependence of the photoluminescence intensity at 1.43, 1.50, 1.65, and 1.84 eV of the spectrum.

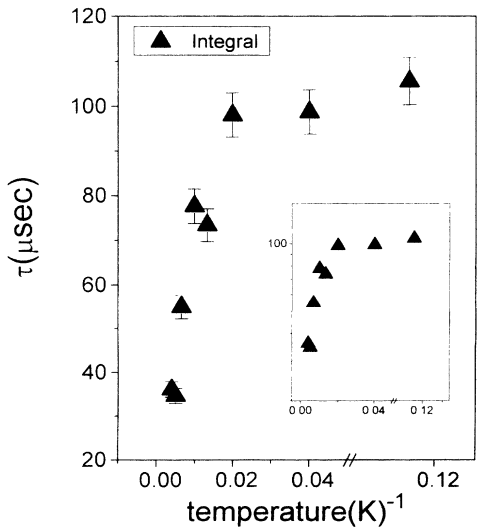

FIG. 11. The measured decay time at 700 nm (1.77 eV) is shown versus inverse sample temperature for sample 1. The inset shows the same data on a logarithmic scale.

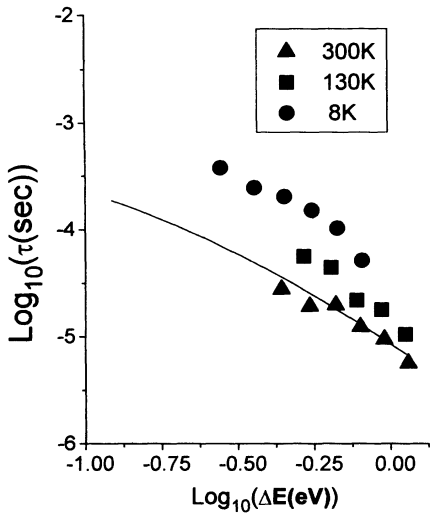

FIG. 12. The measured luminescence decay times are plotted as a function of the blueshift (in eV) for sample 1. The data are shown for $T=8$ K (solid circles), $T=130$ K (solid squares), and $T=300$ K (solid triangles). The solid line is the calculated radiative time due to TO-phonon-assisted transitions at $T=300$ K for nearly cubic crystallites with $f=0.30$.

levels off at ≈ 50 K. The integrated intensity increases by approximately a factor of 10 when the temperature is lowered from 295 to 10 K. The intensity increase is accompanied by about a factor-of-10 decrease in PL decay time, as shown in Fig. 11. We adopt an average method[19] to define a single characteristic time for these generally nonexponential decays[19,20]

$$\tau=\int_0^\infty dt\, I(t)/I(t=0)\ . \tag{6}$$

The implications of the temperature dependence in Fig. 11 for the radiative versus nonradiative channels is discussed below.

For comparison, the radiative rates have been calculated, using Eq. (5b). For the present size range, the TO-phonon-assisted channel dominates[15] and yields radiative decay times in the 10–100 μs range. One should be cautioned that the fine structure in the exciton manifold has not been considered. Therefore, the possibility of slow channels has not been explicitly included.[4] The experimental decay times for several temperatures are compared to the calculated radiative times[21] in Fig. 12. The decay times are from narrow spectra windows, and the horizontal axis is the blueshift relative to the bulk band gap, $E_{\rm PL}$-E_g. The agreement between the calculated radiative times, and the measured decay times at room temperature, is not significant. The latter include parallel nonradiative channels. The situation will be discussed below, but one should note the order-of-magnitude agreement, as well as the general similarity in the shapes of the curves.

V. DISCUSSION

From the combined studies of optical transmission, SRPL, x ray, and TEM, it is clear that the samples used in this work are composed of an ensemble of Si crystallites with maximum diameter in the range of ≈ 60 Å. In addition, the structure and the optical properties are very uniform throughout the film, which makes this type of film ideal for carrying out combined studies with various experimental techniques. These observations show that the luminescence and the absorption properties are intimately related to the nanometer-size Si clusters. However, because the luminescence efficiency is much less than unity, no conclusion can be made as to the detailed luminescence mechanism involved, e.g., within the crystallite, at the surface, or some minority species such as SiH_x. For example, it is difficult to determine quantitatively the amount of the noncrystalline material present. However, the combined data and model do form a coherent picture based on the model of nanometer-scale Si crystallites.

The model calculation accounts accurately for the magnitude of the absorption with a plausible size distribution, i.e., with diameters of the crystallites around 40–50 Å, plus a thin oxide coating as the sample had been exposed to air for about a month before the TEM study. Furthermore, the blueshift of the absorption between the two samples is indicative of a shift of the entire distribution of crystallites to smaller size. The fact that the absorption coefficient rises smoothly with photon energy (without sharp features) and that the absorption coefficient is small but not zero at the emission peak, is also consistent with emission by the lowest states in the absorbing species. However, the small luminescence efficiency implies emission by a small fraction of the distribution, as illustrated in Fig. 9. This requires most of the crystallites to be dark, e.g., contain defects which lead to rapid nonradiative recombination of the carriers.

The small absorption coefficient at the PL peak energy implies, in this picture, that the oscillator strength associated with the light-emitting states is small. The data on the time decay of the luminescence also contain information on the oscillator strength, or can at least be used to set some bounds. In simple terms, the measured 10–100 μs range at room temperature sets an upper bound on the oscillator strength. Thus, it must be several orders of magnitude smaller than for a conventional dipole-allowed transition (typical radiative decay time of order nanoseconds), e.g., in GaAs material.

The measured decay rate is, of course, the sum of the radiative and parallel nonradiative channels. The temperature dependence of the efficiency places some bounds on the nonradiative fraction, at least that which is strongly sensitive to temperature (the usual assumption). We find that the decay time and intensity have correlated dependence on temperature, with the saturation of both occurring for $T<50$ K. They also exhibit an overall change of about the same factor, five to ten depending on emission energy. Thus, in a conventional picture of the dynamics of photoluminescence, the low-temperature decay times should be representative of the radiative decay times.

Returning to consider Fig. 12, the correct comparison to the model, in this interpretation, is between the solid circles and the solid line. The model predicts an approximate $\Delta E^{-3/2}$ dependence for the phonon-assisted transitions. This traces to the matrix element for phonon-

assisted transitions in Eq. (A1b) of the Appendix, the square of which has a net inverse crystallite volume dependence. Physically, the phonon-assisted transitions are faster for more localized electrons and holes. This shape is in reasonable agreement with the present data, although the calculations suggest a rate that is about five times faster than measured low-temperature decay rates.

To summarize, the basic nanocrystallite model yields the following picture. The red emission is ascribed to radiative recombination of electrons and holes in the lowest "bulk" states of those crystallites which are not poisoned by a fast nonradiative channel. The transition involved has weak oscillator strength and predominantly proceeds with the assistance of a phonon. The agreement of the model, within a factor of 5, for the radiative time is adequate given the crudity of the model. However, some aspects of this simple picture must be examined more critically.

There is a noticeable difference between the present samples and other samples for which low-temperature decays are published in the literature. The low-temperature decay is reported[4] to be anomalously slow. That is, the decay rate slows down by an amount that is more than can be accounted for by changes in efficiency, i.e., quenching of nonradiative channels. This is also reported for dispersed Si nanocrystallites.[6] We have observed similar behavior for other preparations of porous Si. One model for this anomalous slowing down invokes a low-energy splitting of the exciton manifold, with a magnitude of order 100 K and with the lowest-lying exciton having even weaker oscillator strength.[4] This has not been explicitly treated here, but it is a plausible model. One reason for not observing this here may relate to a different sample morphology. Our samples show a consistently redder emission and lower efficiency. It is also possible that there is a temperature-independent nonradiative pathway which shorts out any slow radiative channel. One candidate is a tunneling mechanism.[19]

Another aspect concerns the possibility of traps which could lead to real space separation of electrons and holes. For example, the fast trapping of holes on the surface of CdSe crystallites leads to slower than expected radiative recombination and other complexities in the radiative dynamics.[22] A similar scenario has been extensively discussed for porous Si.[10] This could explain the fact that the measured decay times are slower than those calculated for the bulk recombination in the crystallites. The reduced overlap in Eq. (A4) of the Appendix leads to slower radiative recombination. Given that the difference is less than one order of magnitude, we suggest that the trapping is quite shallow, involving carrier localization on a length scale not too much smaller than the crystallite dimension. Therefore, this need not involve a significant Stokes shift, because reduced electron-hole attraction could compensate the trapping energy to some degree. It is difficult to search for evidence of a Stokes shift or excess absorption (sharp features in the absorption spectrum) due to the surface trap species given the inhomogeneous distribution of crystallite sizes and shapes in a typical sample. More homogeneous samples, with larger-scale crystallites, show evidence for subband gap absorption which has been attributed to a distribution of surface traps.[10] Our measurements also yield an exponential dependence of absorption on energy. The form of the large-size tail of the distribution of sizes can strongly influence the low-energy portion of the absorption. This makes it difficult to draw definitive conclusions. However, our results are not inconsistent with some excess low energy absorption.

It is also unlikely that the slow luminescence decay can be attributed to diffusion of carriers prior to recombination, at least not fully. There is no observable rise time for the luminescence (scale of nanoseconds). However, this could play some role in the longer time tails (nonexponential decay profiles). There are two more possibilities for the observed small absorption coefficient at the PL peak energy. First, there could be a genuine Stokes shift as in some molecular systems.[23] Because of the relatively large size of the clusters as compared to that of the typical molecules, we do not believe that this is a likely scenario. Second, the PL could be due to a small minority phase with strong oscillator strength. However, the slow luminescence decay times argue against such a species having strongly allowed transitions.

Another interesting aspect of the luminescence from porous Si is the recently emphasized blue band.[24,25] It exhibits much faster decay times, typically on the order of nanoseconds. We have also observed such a band, although it is quite weak. At the present time, it is not clear what component of the sample is responsible for this light emission. Also, the observed decay time has not yet been related to the radiative time. The results of Fig. 12 strongly suggest that the blue emission cannot result from recombination of states interior to Si nanocrystallite with a radiative time faster than about 1 μs.

VI. CONCLUSION

The uniformity of the present samples ensures that the absorption measurement is characteristic of the observed structure, which is composed of coated nanoscale Si crystallites. The absorption rises smoothly from threshold. This, together with the agreement with the model calculations, strongly supports the mechanism of absorption being dominated by phonon-assisted transitions in the bulk of the crystallites. The difference between the conclusion one can draw from PL and absorption experiments should be emphasized. A blueshift in the PL spectrum shows that there are likely to be some Si nanoclusters in the sample, whereas a blueshift in the absorption edge shows that nearly the entire sample is composed of nanometer-scale Si crystalalites. The precise luminescence mechanism remains uncertain, although a consistent picture between model and data can be based on the bulk crystallite model. Details of the luminescence dynamics are sufficiently complex, and sample dependent, that a complete picture is not yet possible. However, the absorption data, the luminescence decay data, and the model calculations all point to an optical transition with weak oscillator strength, with phonon-assisted transitions dominant for red emission. The importance of phonon-assisted transitions is consistent with recent observations

of phonon-related fine structure in low-temperature PL.[4]

The weak oscillator strength imposes an upper limit on how fast an incoherent light-emitting device based on this material can operate. Based on the photoluminescence decay rates, this suggests that a modulated device would not extend beyond the MHz regime while retaining high efficiency. This conclusion is broadly supported by the observed optical properties of porous Si as it has been prepared in many laboratories. However, we do not exclude the possibility of finding a procedure which, for example, results in a surface species with strong oscillator strength for optical transitions in the visible range.

ACKNOWLEDGMENTS

We acknowledge many enlightening discussions with L. E. Brus, N. Koshida, V. Petrova-Koch, P. H. Citrin, and M. A. Marcus.

APPENDIX: DETAILS OF THE EFFECTIVE-MASS MODEL

The six electron valleys in Si are treated including the anisotropy with longitudinal mass $0.92m_e$ and transverse mass $0.19m_e$. The hole manifold is replaced by a single threefold degenerate effective band with mass $0.54m_e$. The spin-orbit splitting is not explicitly included because we are interested in an energy scale generally large compared to $\Delta=0.044$ eV. This also requires inclusion of nonparabolicity which is modeled by an energy dependent mass: $m(E)=m^*(1+aE)$ with E measured from the relevant band edge. In order to assess the magnitude of a, the density of states from the standard empirical pseudopotential band structure for bulk Si (Ref. 26) has been calculated, as shown in Fig. 13. By comparison with the effective-mass model, we estimate $a=0.5$ eV^{-1} for the holes and $a=0.3$ eV^{-1} for the electrons where the mass increases with separation from the band edge in both cases. The fit shown actually uses a density-of-states mass for the electrons which is somewhat larger ($0.4m_e$). We use the experimental masses, but take the nonparabolicity from the fit. The barriers are modeled by a potential step of 3 eV and assuming unit band mass, roughly approximating the influence of an oxide coating. Including the finite barrier does not significantly alter the matrix elements, but is important to get the energy scale for the transitions, particularly the excited states. In calculating the absorption, no explicit account will be taken of excitonic effects. Electron-hole interactions will alter the energy scale somewhat, but for small quantum boxes, the oscillator strength will not be substantially changed.

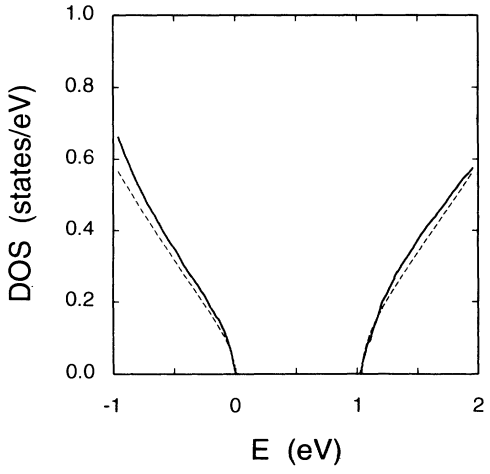

FIG. 13. The calculated pseudopotential density of states for the valence and conduction bands near the fundamental gap of bulk Si (solid lines) is compared to an effective-mass fit of the density of states which includes nonparabolicity (dashed lines).

The matrix elements in Eq. (1) have been analyzed for the crystallite model[15] and have the form

$$p_{eh}^{(1)}=p_{cv}M_{eh}(\mathbf{k}_0)\ , \tag{A1a}$$

$$p_{eh,\lambda\mathbf{q}}^{(2)}=p_{cv}R_\lambda M_{eh}(\mathbf{q}-\mathbf{k}_0)/N_a^{1/2}\ . \tag{A1b}$$

The dipole matrix element for vertical transitions in the bulk crystal p_{cv} enters, and was taken to be independent of $\mathbf{k}$. The electron-phonon interaction enters through the ratio R_λ of the net interaction matrix element and energy denominator, for phonon polarization λ. The vector $\mathbf{k}_0$ is the position of the conduction band edge and $\mathbf{q}$ is the associated phonon wavevector. Confinement effects on the phonon degrees of freedom are not explicitly included, as they will be integrated out below. The number of atoms per crystallite N_a enters explicitly in the phonon-assisted matrix element, but the detailed information about the confined states in the crystallite is carried in

$$M_{eh}(\mathbf{q})=\int d\mathbf{r}\,\psi_e^*(\mathbf{r})\psi_h(\mathbf{r})e^{-i\mathbf{q}\cdot\mathbf{r}}\ . \tag{A2}$$

The wave functions correspond to the envelope functions for the electron and hole states.

The overlap factor in Eq. (A2) has been analyzed previously using an infinite barrier model.[27,28] It is a strong function of both the size and shape of the crystallite and $\mathbf{q}$ with its maximum at $\mathbf{q}=0$. Therefore, in Eq. (A1b), the largest matrix elements are restricted to a range of $\mathbf{q}$ which is close to $\mathbf{k}_0$. For realistic dimensions, that range is less than about 20% of the Brillouin zone size. Then phonon frequencies can be taken to be approximately constant and the sum on $\mathbf{q}$ required in Eq. (1) can be done explicitly:

$$\sum_q \left|M_{eh}(\mathbf{q})\right|^2=\frac{\Omega}{(2\pi)^3}\int d\mathbf{r}|\psi_e(\mathbf{r})|^2|\psi_h(\mathbf{r})|^2 \tag{A3}$$

with Ω the crystallite volume. In this way, the details of the phonon degrees of freedom have been approximately integrated out of the problem.

For the assumed termination by (100)-symmetry surfaces, each electron and hole state decouples into a product form and is labeled by three integers counting the nodes in the envelope portion of the wave function, e.g., $e=(n_{x,e},n_{y,e},n_{z,e})$, plus a valley index for the electrons. The selection rules implied by Eq. (A1a), e.g., for the valley along the x direction, requires $n_{y,e}=n_{y,h}$ and $n_{z,e}=n_{z,h}$. However, all combinations of $n_{x,e}$ and $n_{x,h}$ are allowed. This is a distinct difference from the usual case of a direct band gap semiconductor, which would re-

quire $n_{x,e}=n_{x,h}$ as well. In fact, the overlap factor is an increasing function of the indices $n_{x,e}$ and $n_{h,e}$. The overlap factor as a function of size is illustrated in Ref. 26. The finite barrier model used here has a relatively small influence on the magnitude, so this effect is ignored. The important feature is that the zero-phonon transitions are allowed through the overlap factor Eq. (A2), which is strongly size dependent. The oscillator strength $|p_{eh}^{(1)}|^2$ scales overall roughly as $1/L^6$, with an oscillatory factor that quenches transitions for certain linear dimensions. Also, the only relevant dimension is the one corresponding to the valley orientation. This implies that crystallites of roughly the same volume, but different aspect ratio, can have a rather different zero-phonon oscillator strength for the lowest transition.

The matrix element for the phonon-assisted transitions depends on the electron-phonon interaction. The derivation of Eq. (A1b) relates the needed matrix element to that found in the bulk

$$p_{cv}R_\lambda=\sum_i \frac{\langle v\mathbf{k}|\hat{\mathbf{e}}\cdot\mathbf{p}|i\mathbf{k}\rangle\langle i\mathbf{k}|H_{e\text{-ph}}^{\lambda}|c\mathbf{k}+\mathbf{q}\rangle}{E_{c\mathbf{k}+\mathbf{q}}-E_{i\mathbf{k}}-\hbar\omega_{\lambda\mathbf{q}}} + \sum_j \frac{\langle v\mathbf{k}|H_{e\text{-ph}}^{\lambda}|j\mathbf{k}+\mathbf{q}\rangle\langle j\mathbf{k}+\mathbf{q}|\hat{\mathbf{e}}\cdot\mathbf{p}|c\mathbf{k}+\mathbf{q}\rangle}{E_{v\mathbf{k}}-E_{j\mathbf{k}+\mathbf{q}}-\hbar\omega_{\lambda\mathbf{q}}} . \tag{A4}$$

Here the interaction with the light field is proportional to $\hat{\mathbf{e}}\cdot\mathbf{p}$, the valence state $|v\mathbf{k}\rangle$ is near the zone center, and the conduction state $|c\mathbf{k}+\mathbf{q}\rangle$ is near one of the conduction-band minima at $\mathbf{k}_0$. The matrix element is written for the case of phonon emission. The complementary phonon absorption processes have the same form, with reverse sign for the phonon momentum and energy. The intermediate states must be summed. Then the square matrix element is averaged over the valence-band degeneracy and the conduction-band valley degeneracy. Each phonon polarization gives a distinct channel for absorption or emission with the transverse optic (TO) modes dominant and smaller contributions from the longitudinal-optic (LO) and transverse-acoustic (TA) modes. The case of bulk Si has been extensively studied. The relevant mode energies and corresponding relative intensities are 57.5 meV (1.00), 55.3 meV (0.15), and 18.2 meV (0.03).[29]

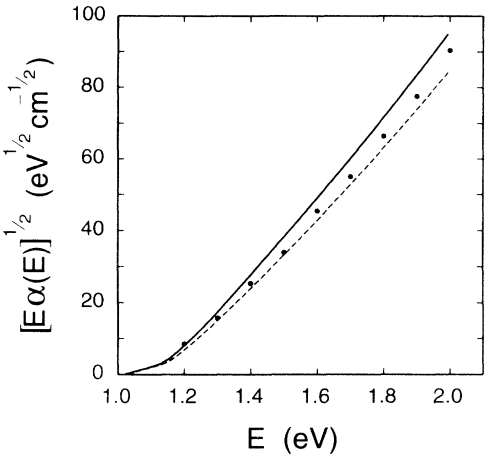

FIG. 14. The calculated absorption at $T=300$ K is compared to the experimental data for bulk Si (Refs. 18 and 30). The solid line is calculated by explicitly convolving the density of states from a pseudopotential band structure (Fig. 13). The dashed line results from an effective-mass model for the density of states, including nonparabolicity. Note that the TA-phonon-assisted transitions are not included.

We determine the oscillator strength for the TO-assisted transitions by comparison to the measured absorption in bulk Si, assuming that the LO contributes 0.15 in intensity, and neglecting the small TA contribution. In terms of the density of states of the valence and conduction band, per spin,

$$\alpha(\hbar\omega)=\sum_\lambda \frac{C_\lambda}{\hbar\omega}\left[(1+n_\lambda)\int_{E_g}^{\hbar\omega-\hbar\omega_\lambda} dE\, D(E)D[E-(\hbar\omega-\hbar\omega_\lambda)]+n_\lambda\int_{E_g}^{\hbar\omega+\hbar\omega_\lambda} dE\, D(E)D[E-(\hbar\omega+\hbar\omega_\lambda)]\right], \tag{A5}$$

where

$$C_\lambda=\frac{32\pi^2}{n}\frac{e^2}{\hbar c}\frac{\hbar^2}{2m_e\Omega_{\text{cell}}}\frac{|p_{cv}|^2}{2m_e}|R_\lambda|^2 \tag{A6}$$

with n the index of refraction and Ω_{cell} the crystal unit-cell volume (per two atoms). Band-structure calculations yield $|p_{cv}|^2/2m_e=4$ eV. The convolved density of states from Fig. 13 is used together with the value of $R_{\text{TO}}=0.067$ in Fig. 14. The agreement with the experimental data[18,30] up to $\hbar\omega=2$ eV, at room temperature, is excellent. The agreement at $T=77$ K is similar. Note that beyond about 2 eV, the next indirect absorption edge near deriving form the L point in the band structure enters. When the effective-mass approximation is used, together with the nonparabolicity indicated above, a slightly larger value of $R_{\text{TO}}=0.08$ is required, and also gives an excellent account of the experimental data (Fig. 14). This value is used in subsequent crystallite calculations.

For the crystallites, the integral in Eq. (A3) also separates into a product of three integrals for the x, y, and z directions. For the infinite barrier model, each contributes a factor of $(2+\delta_{n_{x,e},n_{h,x}})/2$. The volume dependence of the squared matrix element is $1/\Omega$ from the N_a dependence of the electron-phonon interaction. This dominates in Fig. 12. For the case of finite barrier, the

integral should be restricted to the interior Si region, since it is the assumed to be the active portion for the phonon-assisted transitions. The integrals are slightly more complicated, but still can be performed. The quantitative differences are relatively small. One should note that, in general, we have neglected any possible radiative process deriving explicitly from the interface, e.g., due to interface or oxide-derived phonons.

[1]L. T. Canham, Appl. Phys. Lett. **57**, 1046 (1990).

[2]V. Petrova-Koch, T. Muschik, A. Kux, B. K. Meyer, F. Koch, and V. Lehmann, Appl. Phys. Lett. **61**, 943 (1992).

[3]S. L. Friedman, M. A. Marcus, D. L. Adler, Y. H. Xie, T. D. Harris, and P. H. Citrin, Appl. Phys. Lett. **62**, 1934 (1993).

[4]P. D. J. Calcott, K. J. Nash, L. T. Canham, M. J. Kane, and D. Brumhead, J. Phys. Condens. Matter **5**, L91 (1993).

[5]T. Suemoto, K. Tanaka, A. Nakajima, and T. Itakura, Phys. Rev. Lett. **70**, 3659 (1993).

[6]K. A. Littau, P. J. Szajowski, A. J. Muller, A. R. Kortan, and L. E. Brus, J. Phys. Chem. **97**, 1224 (1993); W. L. Wilson, P. F. Szajowski, and L. E. Brus, Science **262**, 1242 (1993)..

[7]H. Takagi, H. Ogawa, Y. Yamazaki, A. Ishizaki, and T. Nakagiri, Appl. Phys. Lett. **56**, 2379 (1990).

[8]S. M. Prokes, W. E. Carlos, and V. M. Bermudez, Appl. Phys. Lett. **61**, 1447 (1992).

[9]R. P. Vasquez, R. W. Fathauer, T. George, A. Ksendzov, and T. L. Lin, Appl. Phys. Lett. **60**, 1004 (1992).

[10]F. Koch, V. Petrova-Koch, T. Muschik, A. Nikolov, and V. Gavrilenko, in *Microcrystalline Semiconductors: Materials Science and Devices,* edited by edited by P. M. Fauchet, C. C. Tsai, L. T. Canham, I. Shimizu, and Y. Aoyagi, MRS Symposium Proceedings No. 283 (Materials Research Society, Pittsburgh, 1993), p. 197; F. Koch, V. Petrova-Koch, and T. Muschik (unpublished).

[11]V. Lehmann and U. Gosele, Appl. Phys. Lett. **58**, 856 (1991).

[12]H. Koyama, M. Araki, Y. Yamamoto, and N. Koshida, Jpn. J. Appl. Phys. **30**, 254 (1991).

[13]Y. Kanemitsu, H. Uto, and Y. Masumoto, Phys. Rev. B **48**, 2827 (1993).

[14]G. E. Carver, Semicond. Sci. Technol. **7**, A53 (1992).

[15]M. S. Hybertsen (unpublished).

[16]C. J. F. Bottcher and P. Bordewijk, *Theory of Electric Polarization,* 2nd ed. (Elsevier, New York, 1978), Vol. II, pp. 476–487.

[17]E. Ettedgui, C. Peng, L. Tsybeskov, Y. Gao, P. M. Fauchet, G. E. Carver, and H. A. Mizes, in *Microcrystalline Semiconductors: Materials Science and Devices,* edited by P. M. Fauchet, C. C. Tsai, L. T. Canham, I. Shimizu, and Y. Aoyagi, MRS Symposium Proceedings No. 283 (Materials Research Society, Pittsburgh, 1993), p. 173.

[18]D. E. Aspnes and A. A. Studna, Phys. Rev. B **27**, 985 (1983).

[19]J. C. Vial, A. Bsiesy, F. Gaspard, R. Herino, M. Ligeon, F. Muller, R. Romestain, and R. M. Macfarlane, Phys. Rev. B **45**, 14 171 (1992).

[20]Y. H. Xie, W. L. Wilson, F. M. Ross, J. A. Mucha, E. A. Fitzgerald, J. M. Macaulay, and T. D. Harris, J. Appl. Phys. **71**, 2403 (1992).

[21]For purposes of calculating the radiative time versus blueshift, two refinements are included. First, the integral in Eq. (A2) is carried out including the finite barrier effects. This introduces an extra, weak size dependence. Second, the blueshift is corrected for an approximate excitonic shift, estimated in first-order perturbation theory. This amounts to approximately -0.2 eV for a net blueshift of 0.5 eV and scales inversely with the dimenision of the crystallite. Also, the local field factor and the overall $\hbar\omega$ in Eq. (5b) introduces partially compensating dependencies on ΔE.

[22]M. G. Bawnedi, W. L. Wilson, L. Rothberg, P. J. Carroll, T. M. Jedju, M. L. Stegerwald, and L. E. Brus, Phys. Rev. Lett. **65**, 1623 (1990).

[23]W. L. Wilson and T. W. Weidman, Phys. Rev. B **48**, 2169 (1993).

[24]D. I. Kovalev, T. Muschik, V. Petrova-Koch, I. D. Yaroshetzkii, and F. Koch, Appl. Phys. Lett. (to be published).

[25]X. Y. Hou, G. Shi, W. Wang, F. L. Zhang, P. H. Hao, D. M. Huang, X. F. Jin, and X. Wang, in *Microcrystalline Semiconductors: Materials Science and Devices,* edited by P. M. Fauchet, C. C. Tsai, L. T. Canham, I. Shimizu, and Y. Aoyagi, MRS Symposium Proceedings No. 283 (Materials Research Society, Pittsburgh, 1993).

[26]M. L. Cohen and J. R. Chelikowsky, *Electronic Structure and Optical Properties of Semiconductors* (Springer-Verlag, New York, 1988).

[27]M. S. Hybertsen, in *Light Emission from Silicon,* edited by S. S. Iyer, L. T. Canham, and R. T. Collins (Materials Research Society, Pittsburgh, 1992), p. 179.

[28]M. Yamamoto, R. Hayashi, K. Tsunetomo, K. Kohno, and Y. Osaka, Jpn. J. Appl. Phys. **30**, 136 (1991); T. Takagahara and K. Takada, Phys. Rev. B **46**, 15 578 (1992).

[29]O. J. Glembocki and F. H. Pollak, Phys. Rev. Lett. **48**, 413 (1982); Phys. Rev. B **25**, 1193 (1982).

[30]W. C. Dash and R. Newman, Phys. Rev. **99**, 1151 (1955).

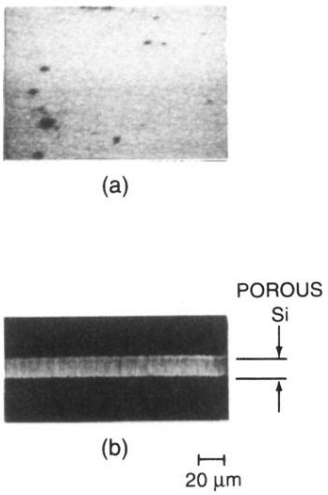

FIG. 2. Spatially resolved photoluminescence (SRPL) scans of sample 1, (a) surface scan, and (b) edge scan.

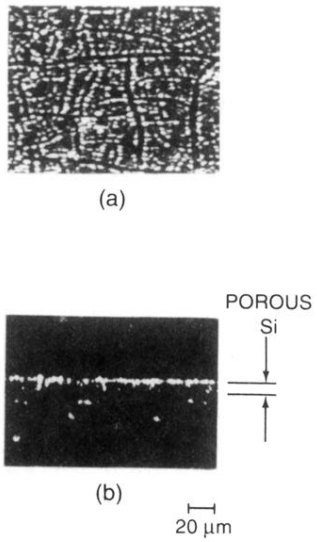

FIG. 3. Spatially resolved photoluminescence (SRPL) scans of a typical porous Si sample which is to lifted off from the substrate; (a) surface scan and (b) edge scan.

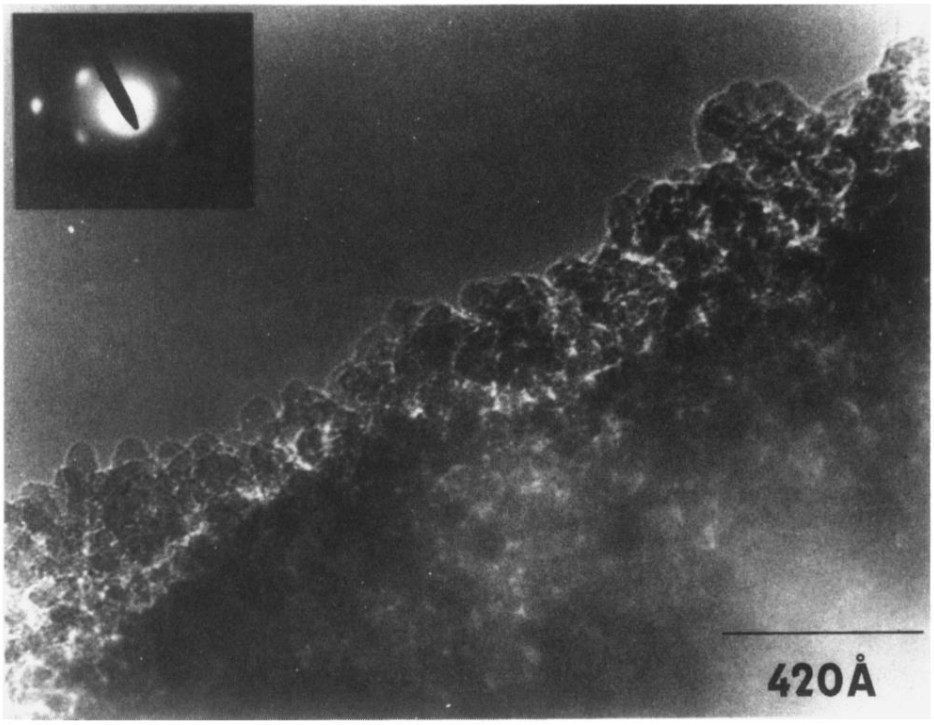

FIG. 5. Phase-contrast transmission electron micrograph of sample 1. The inset shows the diffraction pattern obtained when the beam is restricted to the thin portion of the sample, and its axis is rotated with respect to the micrograph as the result of the electron microscope "lens twist."